Chapter 2
Data Acquisition

In this chapter, we introduce the concept of **resolution** in remote sensing. One common definition of resolution is the ability to discern individual objects or features in a captured image or in the "real world." However, the term also encompasses several specific characteristics of remotely sensed data. We illustrate these specific resolution characteristics with examples of commonly used satellite sensors and imagery. We conclude the chapter with an overview of the types of sensors available to today's analysts, including details about the data they acquire and their potential applications.

Data Resolution

When we talk about "remotely sensed data," we are usually referring to digital images captured by sensors mounted on aircraft or spacecraft. These data are primarily described by four types of resolution: **spatial**, **spectral**, **temporal**, and **radiometric resolution**. **Spatial resolution** is a measure of the fineness of detail of an image. For digital images, this refers to the ground area captured by a single pixel; because pixels are typically square, resolution is generally expressed as the side length of a pixel. **Spectral resolution**, represented by the width of the wavelength interval and/or number of spectral channels (or **bands**) captured by a sensor, defines the storage of recorded electromagnetic energy and the sensor's ability to detect wavelength differences between objects or areas of interest. The amount of time it takes a sensor to revisit a particular geographic location is referred to as its **temporal resolution**. Finally, the sensitivity of a sensor to brightness values (i.e., the smallest differences in intensity that it can detect) is known as its **radiometric resolution**. This metric is usually articulated in terms of binary bit-depth, which refers to number of grayscale levels at which data are recorded by a particular sensor (Jensen 2005). The binary bit-depth is typically expressed in the following ranges of grayscale levels: 8-bit (0–255), 10-bit (0–1,023), 11-bit (0–2,047), 12-bit (0–4,095) and 16-bit (0–65,535).

S. Khorram et al., *Remote Sensing*, SpringerBriefs in Space Development,
DOI: 10.1007/978-1-4614-3103-9_2, © Siamak Khorram 2012

Each of these resolution types is described in greater detail below. But first, the different resolution characteristics of some currently operational satellite sensors are presented in Table 2.1. The sensors described in this table are highly variable with respect to resolution. For example, the Quickbird satellite's onboard sensor has a spatial resolution of 65 cm for **panchromatic** (or black-and-white) imagery, while data collected by the "VEGETATION" sensors on the SPOT 4 and 5 satellites are stored in 1,150-m pixels. Temporally, the sensors listed in Table 2.1 have the capacity to revisit a particular location on Earth's surface every 15 min (i.e., GOES satellites) to every 35 days (i.e., MERIS and other sensors on the Envisat-1 satellite).

The ability to discern spatial structure is an important element of any remote sensing analysis. For instance, in an urban landscape, surface features such as roads, office buildings, parks, and residential neighborhoods comprise a sort of mosaic, where many small constituent units are interspersed with a few large ones. Roads and buildings are typically among the smallest of these units. When viewed from above (e.g., from an airplane), the net visual effect is an aggregate "patchwork" of various land uses and cover types, but the degree of patchwork detail portrayed by a remotely sensed image, and thus the level of specificity at which it can be classified, depends on its spatial resolution (Fig. 2.1). For example, a 30-m pixel (i.e., a spatial resolution provided by several sensors listed in Table 2.1) stores one digital number per spectral band of information for any landscape feature smaller than 900 m^2. The pixel could, in fact, accommodate six one-story square houses, each having a 1500 ft^2 (139 m^2) footprint. In contrast, an Advanced Very High Resolution Radiometer (AVHRR) pixel, with its 1100-m resolution (see Table 2.1), could incorporate more than 8,700 of these houses, if arranged regularly. Increases in spatial resolution have been a persistent trend in sensor innovation. The latest commercial satellites (e.g., GeoEye-1 and WorldView-2) provide spatial resolutions of 1 m or less.

The spectral component of remote sensing data is also critical to appropriate data selection. The spectral resolution of a sensor is a description of the range and partitioning of the electromagnetic energy (or **reflectance**) recorded by the sensor. In this context, sensors can be divided into one of three loose classes of spectral sensitivity: panchromatic (one spectral band), **multispectral** (multiple spectral bands), or **hyperspectral** (many, possibly hundreds, of spectral bands) (Jensen 2005). Fundamentally, both multispectral and hyperspectral images can be thought of as "stacks" of identically geo-referenced (i.e., covering the exact same geographic area) panchromatic images, where each image in the stack corresponds to a particular portion of the electromagnetic spectrum. Conventionally, satellite-derived remote sensing data are captured in panchromatic and/or multispectral format. (Spaceborne hyperspectral imaging, as discussed below, is a relatively recent development). For example, the ETM+ sensor onboard NASA's Landsat-7 satellite records data in eight bands, including one panchromatic band. Each of these bands is sensitive to different wavelengths of visible and infrared radiation. The sensor on the Quickbird satellite records data in four spectral bands targeted at the blue, green, red, and near-infrared portions of the electromagnetic spectrum,

Table 2.1 Characteristics of selected satellite sensors (adapted from Rogan and Chen 2004; updated for this publication)

Sensor (Mission)	Organization[a]	Operation period	Swath width (km)	Spatial resolution (m)[b]	Temporal resolution	Radiometric resolution	Spectral resolution (μm)	Spectral bands
MSS (Landsat 1-5)	NASA, USA	1972–1992	185	80 (MS), 240 (TIR)[c]	16–18 days	8-bit	0.5–1.1, 10.4–12.6[c]	4–5[c]
TM (Landsat 4, 5)	NASA, USA	1982–	185	30 (MS), 120 (TIR)	16 days	8-bit	0.45–2.35, 10.4–12.5	7
ETM+ (Landsat 7)	NASA, USA	1999–	185	15 (PAN), 30 (MS), 60 (TIR)	16 days	8-bit	0.52–0.9 (PAN), 0.45–2.35, 10.4–12.5	7 + PAN
MODIS (EOS Terra and Aqua)	NASA, USA	1999–	2300	250 (PAN), 500 (VNIR), 1000 (SWIR)	1–2 days	12-bit	0.620–2.155, 3.66–14.385	36
ASTER (EOS Terra)	NASA,USA and METI, Japan	1999–	60	15 (VNIR), 30 (SWIR), 90 (TIR)	4–16 days	8-bit (VNIR/SWIR), 12-bit (TIR)	0.52–0.86, 1.60–2.43, 8.125–11.65	14
Hyperion (EO-1)	NASA, USA	2000–	7.5	30	16 days	12-bit	0.353–2.577	220
ALI (EO-1)	NASA, USA	2000–	37	10 (PAN), 30 (MS)	16 days	12-bit	0.48–0.69 (PAN), 0.433–2.35	9 + PAN
CALIOP (CALIPSO)	NASA, USA and CNES, France	2006–	0.1	333	16 days	22-bit[d]	0.532, 1.064	2[e]
AVHRR (NOAA 6-19)	NOAA, USA	1978–[f]	2700	1100	12 h	10-bit	0.58–12.5	6[g]
I-M Imager (GOES 11-15)	NESDIS, USA	1975–[h]	8	1000 (VNIR), 4000 (SWIR), 8000 (moisture), 4000 (TIR)	0.25–3 h	10-bit	0.55–12.5	5
SAR (RADARSAT-1)	CSA, Canada	1995–	45–500[i]	8–100[i]	24 days		Radar	N/A
SAR (RADARSAT-2)	CSA, Canada	2007–	20–500[i]	3–100[i]	24 days[j]		Radar	N/A
MERIS (Envisat-1)	ESA	2002–	1150	300 (land), 1200 (ocean)	35 days[k]	12-bit	0.39–1.04	Up to 15
AATSR (Envisat-1)	ESA	2002–	500	1000	35 days[k]	12-bit	0.55–12	7
ASAR (Envisat-1)	ESA	2002–	100–400[i]	30–1000[i]	35 days[l]		Radar	N/A
HRC (CBERS-2B)	CBERS, China/Brazil	2007–	27	2.7	26 days	8-bit	0.45–0.85	1
CCD (CBERS-2B)	CBERS, China/Brazil	2007–	113	20	26 days	8-bit	0.45–0.73	5
TANSO-FTS (GOSAT/Ibuki)	JAXA, Japan	2009–	160[m]	10.5	3 days		0.758–14.3	4
LISS-4 (RESOURCESAT-2)	ISRO, India	2011–	70	5.8	24 days	10-bit	0.52–0.86	3
LISS-3 (RESOURCESAT-2)	ISRO, India	2011–	141	23.5	24 days	10-bit	0.52–1.70	4
AWiFS (RESOURCESAT-2)	ISRO, India	2011–	740	56	24 days	12-bit	0.52–1.70	4

(continued)

Table 2.1 (continued)

Sensor (Mission)	Organization[a]	Operation period	Swath width (km)	Spatialresolution (m)[b]	Temporal resolution	Radiometric resolution	Spectral resolution (μm)	Spectral bands
HRVIR (SPOT 4,5)	SPOT Image, France	1998–	60	10 (PAN), 20 (MS)	26 days[n]	8-bit	0.61–0.68 (PAN), 0.50–1.75	4 + PAN
VEGETATION (SPOT 4,5)	SPOT Image, France	1998–	2250	1150	26 days[n]	10-bit	0.43–1.75	4
HRG (SPOT 5)	SPOT Image, France	2002–	60	2.5–5 (PAN), 10 (VNIR), 20 (SWIR)	26 days[n]	8-bit	0.48–0.71 (PAN), 0.50–1.75	4 + PAN
IKONOS	GeoEye, USA	1999–	11.3	1 (PAN), 4 (MS)	3–5 days	11-bit	0.526–0.929 (PAN), 0.445–0.853	4 + PAN
Quickbird	DigitalGlobe, USA	2001–	18	0.65 (PAN), 2.62 (MS)	2.5–5.6 days	11-bit	0.405–1.053 (PAN), 0.43–0.918	4 + PAN
GeoEye-1	GeoEye, USA	2008–	15.2	0.41 (PAN), 1.65 (MS)	<3 days	11-bit	0.45–0.80 (PAN), 0.45–0.92	4 + PAN
WorldView-2	DigitalGlobe, USA	2009–	16.4	0.46 (PAN), 1.85 (MS)	1.1–3.7 days	11-bit	0.45–0.80 (PAN), 0.45–1.04	8 + PAN

[a] Organization acronyms: *NASA* National Aeronautics and Space Administration, *METI* Ministry of Economy, Trade, and Industry, *CNES* Centre National d'Études Spatiales, *NOAA* National Oceanic and Atmospheric Administration, *NESDIS* National Environmental Satellite, Data, and Information Service, *CSA* Canadian Space Agency, *ESA* European Space Agency, *CBERS* China-Brazil Earth Resources Satellite Program, *JAXA* Japanese Aerospace Exploration Agency, *ISRO* Indian Space Research Organization

[b] Acronyms used in describing sensor channels/configurations: *MS* multispectral, *TIR* Thermal infrared, *PAN* Panchromatic, *VNIR* Visible and near-infrared, *SWIR* Short-wave infrared

[c] The MSS sensor on Landsat 3 had a fifth spectral band for thermal infrared. The MSS sensors on other Landsat missions had four-band configurations

[d] Each receiver channel on the CALIOP sensor, a spaceborne LiDAR system, has dual 14-bit digitizers that jointly provide a 22-bit dynamic range

[e] The CALIOP sensor produces simultaneous laser pulses at two wavelengths, 0.532 and 1.064 μm

[f] The NOAA satellite program began in 1978. Currently, NOAA-19 is designated as the program's "operational" satellite, while NOAA-15, NOAA-16, NOAA-17, and NOAA-18 still transmit data as "standby" satellites

[g] While the AVHRR sensor has six spectral channels, only five are transmitted to the ground at any time. The bands designated 3A and 3B are transmitted only during daytime and nighttime, respectively

[h] Although the GOES satellite program has been active since 1975, only GOES-11 through GOES-15 are currently operational. GOES-11 was launched in 2000 but put into operation in 2006, replacing an earlier GOES satellite

[i] The radar systems in this table (i.e., RADARSAT-1, RADARSAT-2, and ASAR) operate in a variety of scan modes with different swath widths and spatial resolutions

[j] RADARSAT-2 has a repeat cycle of 24 days, but its left- and right-looking modes may provide more rapid revisits

[k] The orbit cycle of the Envisat-1 satellite is 35 days. The wide swaths of the MERIS and AATSR sensors permit more rapid revisits (approximately every three and every six days, respectively), but images are captured from different orbits and thus have different observation geometry, which may affect image processing

[l] The repeat cycle of the Envisat-1 satellite is 35 days, but more rapid revisits are possible with the ASAR depending on the latitude of the area of interest, requirements regarding the incidence angle (i.e., the angle between the radar beam and a line perpendicular to the ground), and desired scan mode

[m] The FTS sensor on the GOSAT satellite records 10.5 × 10.5 km images that, nominally, are spaced 150 km apart in a grid (see Kuze et al. 2009)

[n] The SPOT satellites have the capacity to record data off-nadir (i.e., to record data in areas that are not directly below the satellite). This may reduce revisit time to 2–3 days (1 day for the wide-swath VEGETATION sensor), but the images will have different observation geometry, which may affect image processing

Fig. 2.1 Landsat ETM+ (*left*) and Quickbird (*right*) images of the same area, demonstrating the large difference in spatial resolution between the two sensors (Landsat ETM+ multispectral resolution = 30 m; Quickbird multispectral resolution = 2.62 m). In the Quickbird image, individual buildings and minor road features are readily discernible

Table 2.2 Comparison of the spectral resolutions of the Landsat ETM+ and Quickbird sensors

Bandwidth (μm)		
Spectral band	Landsat ETM+[a]	Quickbird
Panchromatic	0.52–0.9	0.405–1.053
Blue	0.45–0.515	0.43–0.545
Green	0.525–0.605	0.466–0.62
Red	0.63–0.69	0.59–0.71
Near-infrared	0.75–0.9	0.715–0.918
Mid-infrared	1.55–1.75	
Thermal infrared	10.4–12.5	
Mid-infrared	2.09–2.35	

[a] The ETM+ sensor is configured with two mid-infrared bands, designated bands 5 and 7, on either side of band 6, a thermal infrared band

as well as a panchromatic band. Table 2.2 compares the spectral bandwidths of the Landsat ETM+ and Quickbird sensors. Notably, in many geographic areas, ambient electromagnetic reflectance is strongly shaped by the distribution and condition of vegetation and water features, especially in the **visible to near-infrared** (**VNIR**) range (0.4–1.4 μm) of the electromagnetic spectrum to which many of the sensors in Table 2.1 are attuned.

Alternatively, NASA's Hyperion sensor, the first spaceborne hyperspectral sensor, provides a virtually continuous recording of electromagnetic reflectance across 220 narrow spectral bands in the VNIR and **short-wave infrared** (**SWIR**) wavelengths. Although the processing complexity of hyperspectral data has hindered its applicability in many land cover studies, these data provide a great deal of information about the unique reflectance behavior of vegetation stress and diversity. The high spectral resolution also provides an increased ability to

discriminate between features that have similar response profiles, or **signatures**, across the electromagnetic spectrum, such as forest stands composed of different deciduous tree species (Chen and Hepner 2001).

Often, temporal resolution, or revisit time, is expressed in terms of days. For example, Landsat-7 has a 16-day orbit cycle, meaning that the satellite (and its ETM+ sensor) returns to a given location on Earth's surface every 16 days. However, some satellites, such as the Geostationary Operational Environmental Satellites (GOES), have a revisit cycle of less than an hour in certain locations. The GOES satellites, which are most commonly associated with meteorology and climate research, have a coarse, 8-km spatial resolution which gives them limited utility for local land cover studies. By contrast, the balance of spatial and temporal resolution achieved by NASA's Moderate Resolution Imaging Spectroradiometer (MODIS)—with a spatial resolution of 250–1000 m and a temporal resolution of 1–2 days—has made the sensor applicable to a variety of regional- to continental-scale research efforts.

In addition to the high spatial resolutions possible with commercial satellites such as WorldView-2, their onboard sensors also have high radiometric resolutions. Their 11-bit collection depth represents a substantial improvement over the 8-bit resolution typically exhibited by predecessors such as the Landsat sensors. Radiometric resolution refers to the **dynamic range** (i.e., the number of possible data values) recorded in each image band. Higher radiometric resolution means that a sensor is more sensitive to variations in electromagnetic reflectance (Fig. 2.2). This increased sensitivity has been shown to be very useful in the land cover classification of complex (i.e., urban and suburban) landscapes (Hester et al. 2008, 2010).

Ultimately, each of the four resolution types must be considered in light of the intended purpose of the data. For example, except near cities, most terrestrial landscapes are dominated either by vegetation, water, or other natural surfaces, even amid production land uses such as agriculture or mining. Spatial resolution might be relatively less important for mapping or monitoring efforts in these settings because of high landscape homogeneity. In heavily vegetated environments, data that are high in temporal and spectral resolution rather than spatial resolution, such as AVHRR imagery, could be a powerful tool for evaluating seasonal or annual change in photosynthetic activity (Moulin et al. 1997; Stöckli and Vidale 2004). With respect to other types of analyses, hyperspectral data have demonstrated strong applicability for geological, mineralogical, and soil studies (e.g., Galvão et al. 2008; Weber et al. 2008). In addition, **radar** systems such as the Advanced Synthetic Aperture Radar (ASAR) on the Envisat-1 satellite can be useful for observing changes in sea surface conditions (Johannessen et al. 2008), while one of the major applications of Envisat-1's Medium Resolution Imaging Spectrometer (MERIS) sensor is for studying changes in ocean color (Cui et al. 2010). In short, there is no one "best" sensor for mapping a particular type of landscape. Although the sensors listed in Table 2.1 are only a sample of the instruments currently producing remotely sensed data, they illustrate the wide diversity of options that an analyst should consider before choosing a particular sensor.

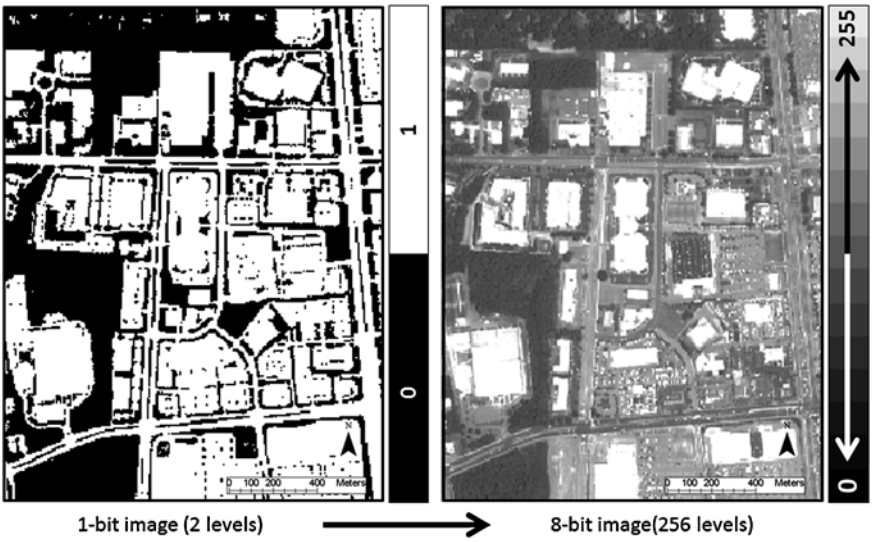

Fig. 2.2 The concept of radiometric resolution is illustrated by two images. The image on the left represents a 1-bit image, where two *brightness* values, or *grayscale* levels (i.e., *black* and *white*), are portrayed within the data. The image on the right represents an 8-bit image, where up to 256 *grayscale* levels are portrayed within the data. In contrast to these images, an 11-bit image holds up to 2,048 *grayscale* levels

Payloads and Platforms: An Overview

In remote sensing, the carrier of a sensor is known as its **platform**, while the sensor itself is the platform's **payload**. Remote sensing platforms are split into two categories: airborne and spaceborne. During the last two decades, there has been rapid proliferation of platforms in both categories. Here, we provide a brief overview of major platforms and sensor formats in use historically and today.

Airborne Platforms

Although the primary focus of this book is satellite-based remote sensing and the processing of associated digital data, until the emergence of satellite imagery in the 1970s, aerial photography served as the main data source when mapping phenomena on Earth's surface (Short 2010). Through time, "true" color and color-infrared film became economically feasible as alternatives to panchromatic film, and offered better capability for tasks such as vegetation classification (Caylor 2000). Until recently, digital cameras did not provide the same level of fine detail as film-based cameras, but many currently available digital aerial cameras have comparable spatial resolutions to film cameras, with similar formatting and scale (Morgan et al. 2010).

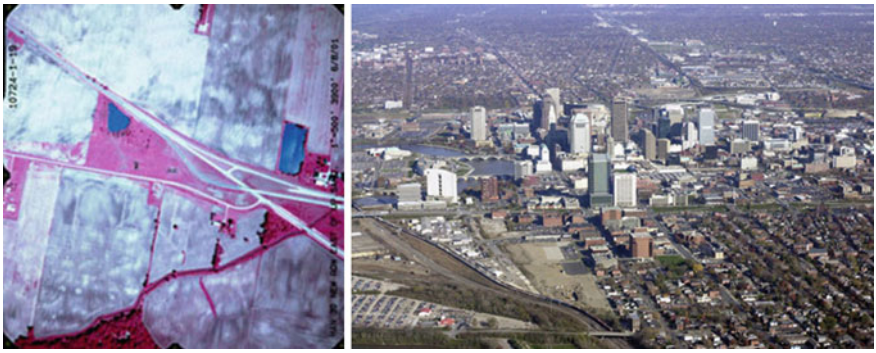

Fig. 2.3 A vertical aerial photograph (*left*) and an oblique aerial photograph (*right*). Images courtesy of Ohio Department of Transportation

Aerial photography may be either **vertical** or **oblique** (Fig. 2.3), depending on the orientation of the camera's optical axis relative to Earth. Vertical photos are captured with the camera's axis at an angle perpendicular or near-perpendicular ($90^o \pm 3^o$) to the ground. Oblique photos are typically captured with the camera's axis tilted more than 20^o from vertical.

Because airborne platforms are not suited to capturing large geographic areas (e.g., 10,000 km^2) at once, they have been replaced by spaceborne platforms for most broad-scale remote sensing projects (Short 2010). Nevertheless, aerial photography remains viable because it can be tailored to specific project needs (e.g., a particular spatial scale or resolution) in ways that satellite imagery cannot (Morgan et al. 2010). Aerial photography continues to be the foundation of many national-scale mapping efforts, such as the National Agricultural Imagery Program (NAIP), which has the goal of providing regularly updated, geo-referenced imagery to the public (USDA FSA 2010). In addition, the development of image processing techniques for satellite imagery has in turn expanded the range of automated techniques that may be applied to digital aerial photos (Morgan et al. 2010), including **object-oriented classification** (see Chap. 3). Various non-photographic sensors have also been implemented via airborne platforms, including **active remote sensing systems** such as radar and **LiDAR**. Radar (short for RAdio Detection and Ranging) systems operate within the microwave portion of the electromagnetic spectrum (Lillesand et al. 2008). Essentially, a radar sensor works by emitting radio waves from an antenna that bounce off target features on Earth, and then the sensor records the returned energy. The target features may be distinguished from one another by their differing effects on the returned signals. Radar sensors can capture images day or night, and in all weather conditions (e.g., through cloud cover or smoke). For this reason, radar imaging is often used in disaster management, for instance in detecting ocean oil spills (Jha et al. 2008; Klemas 2010). Radar **interferometry** involves the simultaneous use of two antennae to generate radio waves and collect returned signals; incorporating the distance between these antennae during data processing facilitates topographic

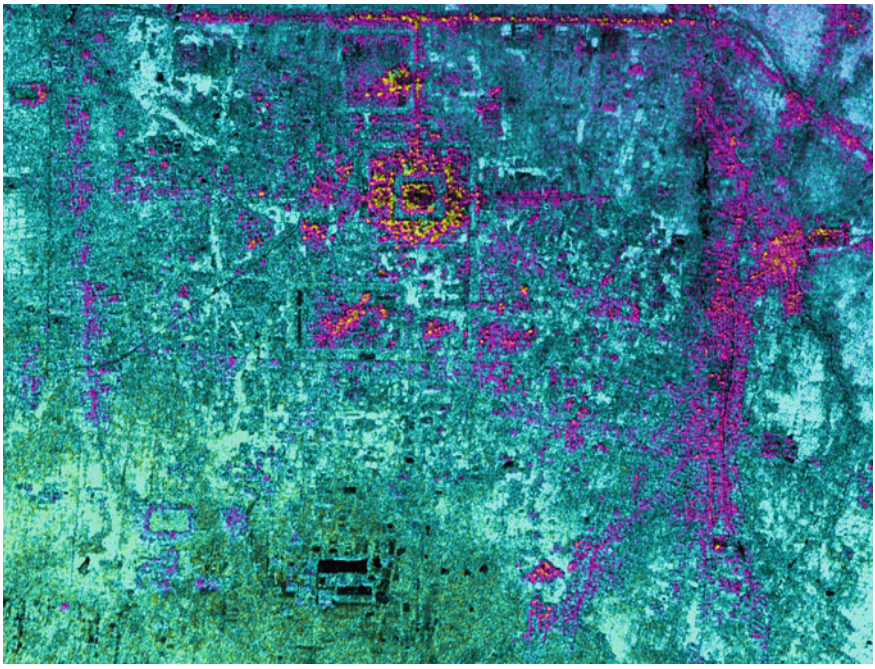

Fig. 2.4 Topographic image of Hariharalaya, the nineth century capital of the Khmer Empire in Cambodia. The image was captured by the NASA Airborne Synthetic Aperture Radar (AIRSAR) sensor, operating in interferometric mode. Colors represent elevation contours. Image courtesy of NASA Jet Propulsion Laboratory

mapping (Massonnet and Fiegl 1998). For instance, Fig. 2.4 shows an application of airborne radar interferometry to develop a **digital elevation model**, or **DEM**, of the area surrounding an ancient city site in Cambodia.

LiDAR (short for Light Detection And Ranging) systems resemble radar in that the output images are generated based on the amount of sensor-emitted energy that is returned from features on the ground. However, unlike radar, LiDAR sensors emit laser pulses (typically in the near-infrared portion of the electromagnetic spectrum) at a very high rate (i.e., 10,000–100,000 pulses per second) (Reutebuch et al. 2005). In turn, the three-dimensional positions of targeted objects are determined based on the time it takes for pulses to return the sensor. The typical LiDAR output image is a topographic data set with very accurate vertical measurements (± 10–15 cm error) (Charlton et al. 2003; Reutebuch et al. 2005). Most airborne LiDAR systems can record multiple returns (Fig. 2.5a) from the same laser pulse in cases where an object does not completely block the pulse's path, allowing it to continue to another object closer to the ground (Reutebuch et al. 2005). This feature makes LiDAR systems useful for applications such as the characterization of forest canopy structure (Fig. 2.5b) (Reutebuch et al. 2005; Lim et al. 2003). However, LiDAR systems are sensitive to weather and other conditions that interfere with the laser pulses.

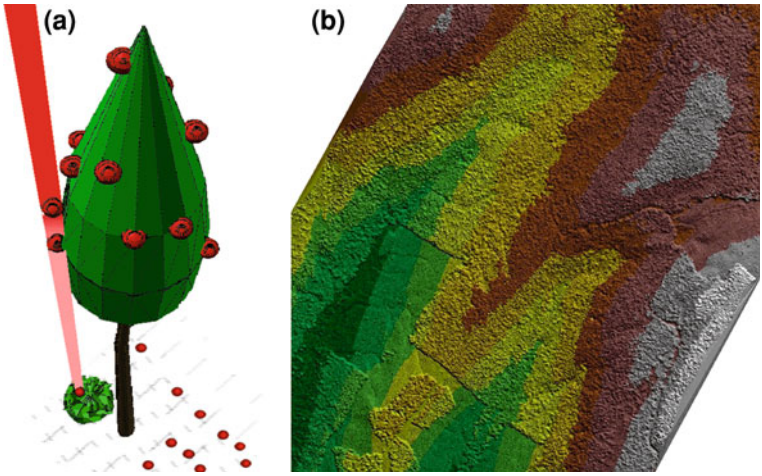

Fig. 2.5 **a** Conceptual rendering of multiple returns from a single laser pulse from an airborne LiDAR system. **b** Forest canopy surface recorded by LiDAR; colors indicate elevation contours. Image credit: Mississippi State University, College of Forest Resources, Measurements & Spatial Technologies Laboratory

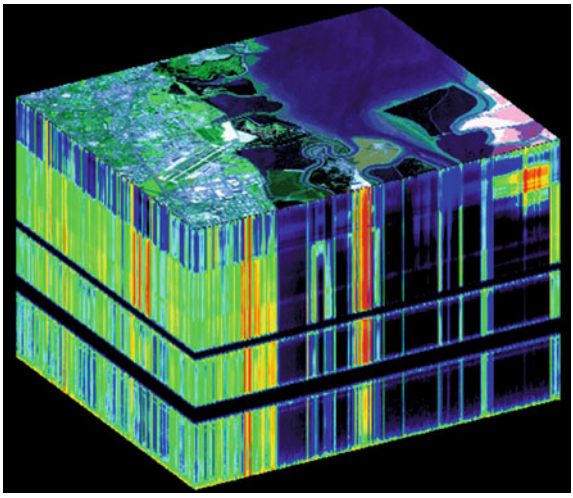

Fig. 2.6 A hyperspectral image data "cube" of Moffit Field, California, captured by the AVIRIS sensor. Moffit Field is at the southern end of San Francisco Bay. The top of the image cube is a false color composite showing evaporation ponds (*center* and *lower right*) as well the Moffit Field airport (*left*). The sides of the cubes show the edges of each image corresponding to one of the sensor's 224 spectral bands. Image courtesy of NASA Jet Propulsion Laboratory

For the past few decades, multispectral scanners resembling the passive sensors found on many Earth-observing satellites have been mounted on airborne platforms. More recently, there has also been increased application of airborne hyperspectral sensors. For example, the AVIRIS (Airborne Visible Infrared Imaging Spectrometer) instrument (Fig. 2.6), operated by NASA, collects data from 224 contiguous bands spanning the ultraviolet to near infrared; the spectral resolution of each AVIRIS band is approximately 0.01 μm. This high degree of

spectral resolution enables analysts to make subtle distinctions regarding objects or areas of interest that are not possible with multispectral data. For instance, hyperspectral imagery has been used to detect early stages of forest damage and decline caused by air pollution (Campbell et al. 2004). However, because of the very large data volume associated with the typical hyperspectral image, an analyst must often use statistical techniques (e.g., principal components analysis) to reduce the dimensionality prior to further image processing (Harsanyi and Chang 1994).

Spaceborne Platforms

An exhaustive list of all Earth-observing satellites that are currently in operation is beyond the scope of this book. Instead, we provide basic details about some prominent government and commercial satellites from the U.S. and elsewhere (mostly listed in Table 2.1). We also highlight promising developments in spaceborne remote sensing (e.g., the availability of satellite-based hyperspectral and LiDAR sensors).

NASA Satellites and Satellite Programs

Essentially, satellite remote sensing began with NASA's Landsat Program. Landsat-1, launched in 1972, was the first in a series of satellites associated with the long-running program, the latest being Landsat-7, launched in April 1999 (Short 2010; Jensen 2005). Besides, Landsat-7, only Landsat-5 (launched in March 1984) remains operational. Both Landsat-5 and Landsat-7 have a 16-day revisit time.

Landsat-5's primary on-board sensor, the Thematic Mapper (TM), was the predecessor of the Enhanced Thematic Mapper (ETM+) on Landsat-7. The ETM+ sensor incorporates two major improvements on the TM sensor: a higher-resolution thermal infrared band (60 m versus 120 m for the TM sensor) as well as the novel inclusion of a 15-m panchromatic band. The ETM+ sensor requires roughly 11,000 scenes to completely image Earth, excluding the polar regions (Short 2010).

With its various sensors, the Landsat Program has provided the longest—by far—continuous and comprehensive record of Earth imagery. Each spectral band of the ETM+ sensor has utility for certain environmental applications (Table 2.3). Figure 2.7 is an ETM+ image of the Ganges River Delta; this false-color composite was made using green, infrared, and blue wavelengths. In addition, the entire Landsat image archive has been made available to the public via the Internet, facilitating long-term change analyses.

Landsat-7 is considered part of NASA's Earth Observing System (EOS) mission, which also includes the paired satellites Terra (launched December 1999) and Aqua (launched May 2002). Together, the Aqua and Terra satellites cover the mid to higher latitudes of Earth four times daily. Both satellites carry the Moderate Resolution Imaging Spectroradiometer (MODIS) sensor. The MODIS sensor

Table 2.3 Capabilities and applications of ETM+ spectral bands (adapted from Jensen 2005)

Band	Capabilities/Applications
Band 1 (blue)	Penetrating water bodies; analysis of land-use, soil, and vegetation
Band 2 (green)	Green reflectance of healthy vegetation
Band 3 (red)	Vegetation discrimination; delineation of soil and geologic boundaries
Band 4 (near-infrared)	Crop identification; emphasizes soil–crop and land–water contrasts
Band 5 (mid-infrared)	Drought studies; discrimination between clouds, snow, and ice
Band 6 (thermal infrared)	Locating geothermal activity; vegetation stress analysis; soil moisture studies; detection of urban heat islands
Band 7 (mid-infrared)	Discrimination of geologic rock formations

records data in 36 spectral bands spanning the visible to thermal infrared, with a unique configuration: bands 1 and 2 have spatial resolutions of 250 m, bands 3–7 have spatial resolutions of 500 m, and bands 8–36 have spatial resolutions of 1 km. MODIS data have wide applicability in terrestrial, atmospheric, and marine contexts, primarily for broad-scale (i.e., continental-scale) analyses; some of these applications are highlighted in Chaps. 4, 5 and 6.

The Advanced Spaceborne Thermal Emission and Reflection Radiometer (ASTER) sensor aboard EOS Terra is actually a combination of three radiometers that yield simultaneous and co-registered image data of differing spatial resolutions: three VNIR bands with a spatial resolution of 15 m; six SWIR bands with a spatial resolution of 30 m; and five TIR bands with a spatial resolution of 90 m. While ASTER imagery has regularly been used to study land surface temperature and thermal phenomena such as surface emissivity (e.g., Schmugge et al. 2002), it has also been applied for urban land cover classification (Chen et al. 2007).

NASA launched Earth Observing-1 (EO-1) satellite into orbit in November 2000. Of its various instruments, the Hyperion imaging spectrometer, with its 220 spectral bands, is of particular note. Hyperion data have been used for applications such as analysis of desertification (Asner and Heidebrecht 2003) and the detection of fungal disease in sugarcane (Apan et al. 2004). Figure 2.8 is a Hyperion image, captured in October 2007, of a large wildfire complex in northern San Diego County, California; using three short-wave infrared channels, the sensor was able to cut through dense smoke plumes to show the locations of actively burning fires. However, Hyperion data tend to have a higher signal-to-noise ratio relative to data from airborne hyperspectral sensors such as AVIRIS, which limits their utility for fine-scale mapping and classification (Apan 2004; Kruse et al. 2003). Future spaceborne hyperspectral sensors will likely include technological improvements to address this signal-to-noise ratio limitation.

In May 2003, the ETM+ sensor aboard Landsat-7 experienced a failure of its scan-line corrector (SLC) mechanism. This uncorrectable failure results in data gaps on the left and right sides of each recorded image (Williams et al. 2006). These data gaps are filled using data from another ETM+ image captured close in

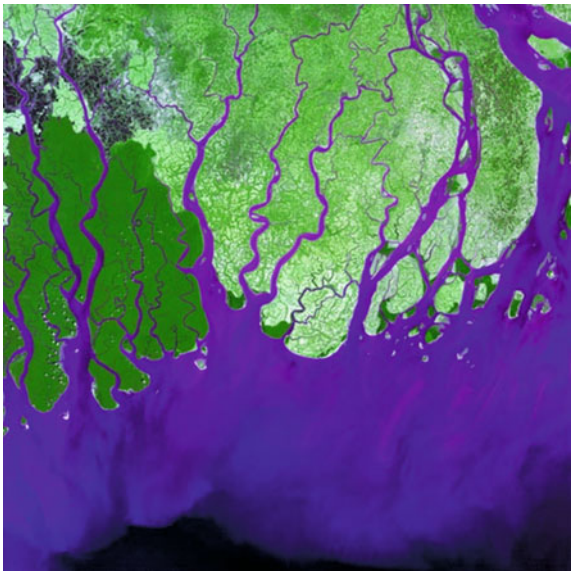

Fig. 2.7 Landsat ETM+ image of the Ganges River Delta, captured in February 2000. The delta is dominated by swamp forest. Image courtesy of U.S. Geological Survey, EROS Data Center, Satellite Systems Branch

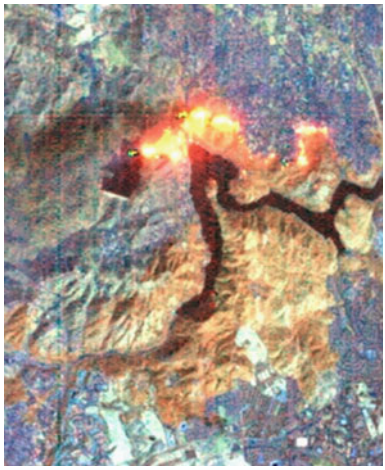

Fig. 2.8 Hyperion image of the Witch Wildfire in northern San Diego County, California, captured in October 2007. Image courtesy of NASA EO-1 Team

time, but the SLC problem—combined with the fact that the only other operational Landsat satellite, Landsat-5, is approaching 30 years of service—emphasizes that the Landsat mission is likely approaching its end. Another sensor on board the EO-1 satellite, the Advanced Land Imager (ALI), was developed as a prototype for sensors that could be carried on future Landsat missions (Chander et al. 2004).

The CALIPSO satellite is jointly operated by NASA and Centre National d'Études Spatiales (CNES), the French government space agency. A key instrument on CALIPSO is the Cloud-Aerosol LiDAR with Orthogonal Polarization (CALIOP) sensor, which represents one of very few operational space-borne

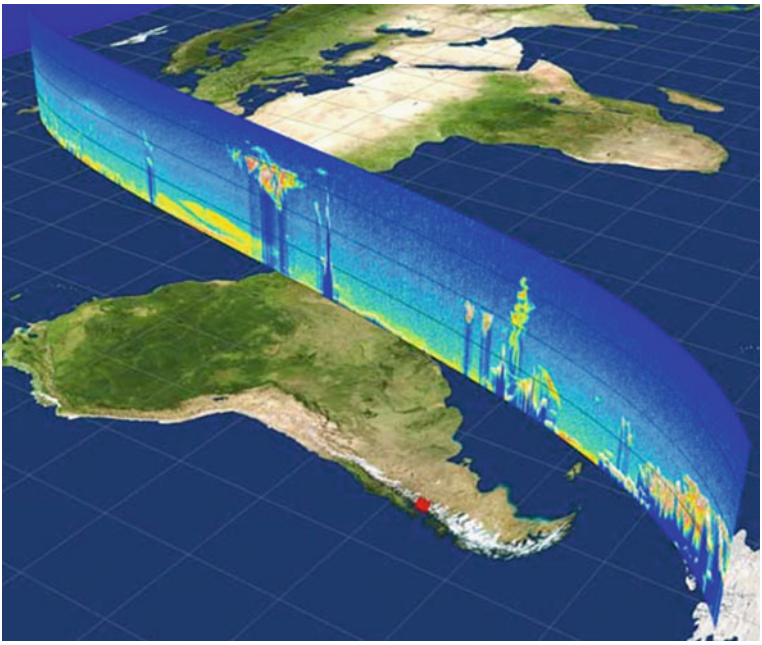

Fig. 2.9 CALIOP image showing vertical profile of ash and aerosols arising from the May 6, 2008 eruption of Chile's Chaitén volcano (*red square*). The top of the aerosol column is approximately 16 km altitude. Image courtesy K. Severance and C. Trepte, NASA Langley Research Center

LiDAR systems. As its name suggests, the CALIOP sensor is used for analysis of a variety of atmospheric phenomena, including dust storms (Liu et al. 2008). Figure 2.9 is a CALIOP image captured May 7, 2008, the day after an eruption of Chile's Chaitén Volcano. Among the phenomena detected by CALIOP was the presence of aerosols in the stratosphere, drifting over southeastern Australia, which suggests rapid, long-distance transport of fine ash (Carn et al. 2009).

Other Government Satellites and Satellite Programs

The **Advanced Very High Resolution Radiometer (AVHRR)** is a sensor mounted on a series of satellites operated by the U.S. National Oceanic and Atmospheric Administration (NOAA). The latest in the series, NOAA-19, was launched in 2009. NOAA-19 carries the third version of the AVHRR sensor, with six spectral bands. Only five bands are transmitted to the ground at any given time; the bands designated 3A and 3B are transmitted during daytime and nighttime, respectively. The AVHRR sensor was primarily developed for oceanographic and meteorological applications, but it has also been used for land cover mapping at broad scales (e.g., Loveland et al. 2000), especially because of its twice-a-day temporal coverage (Jensen 2005).

The NOAA satellites have **polar orbits**, meaning that they pass over the North and South Poles during each trip around Earth. Many other satellites, such as Landsat-7, have **near-polar orbits**. Polar- and near-polar-orbiting satellites are typically **sun-synchronous**, which means that the satellite passes over a given location on Earth at approximately the same local time each day. This characteristic enables regular data collection at consistent times as well as long-term comparisons.

Alternatively, some satellites are placed into a **geostationary orbit**, where the satellite remains fixed in a particular location above Earth (commonly the Equator), and orbits in the direction (and at the speed) of the planet's rotation. One advantage of geostationary satellites is that it easy for ground-based antennae to communicate with them. For this reason, this is the preferred orbit for many weather monitoring satellites, including the Geostationary Operational Environmental Satellite (GOES) system, which serves as the primary information source for the U.S. National Weather Service. The sensor (i.e., the I-M Imager instrument) aboard each GOES satellite records individual images covering approximately 25% of Earth's surface (Jensen 2005). Currently, five GOES satellites are active: GOES-11, designated "GOES West", which is located at 135° W longitude; GOES-12, located at 60° W and currently tasked with imaging South America; GOES-13, designated "GOES East", which is situated at 45° W; GOES-14, which is in on-orbit storage status; and GOES-15, which is on stand-by (NOAA 2011).

The Canadian Space Agency (CSA) launched its first Earth-observing satellite, RADARSAT-1, in November 1995, followed by the launch of RADARSAT-2 in December 2007. The primary payload on each of these satellites is a **synthetic aperture radar** (**SAR**) imaging system. A SAR system utilizes the motion of the platform that carries it (e.g., a satellite) to simulate a large antenna, or aperture. In short, as the platform moves, the system transmits multiple, successive radio pulses toward targeted objects or areas. The returned signals are then synthesized into a single image with higher spatial resolution than could be captured with a smaller, physical antenna.

The RADARSAT satellites have the all-weather capabilities of airborne radar systems, but with the added advantage of frequent revisits (every 24 days) of targeted areas. (RADARSAT-2 has side-looking modes that can further reduce revisit time.) The SAR systems on the RADARSAT satellites also have multiple beam modes that essentially trade swath size for improved spatial resolution. A particular strength of satellite-based SAR imagery is the ability to measure ocean waves and currents over large areas (Goldstein et al. 1989); for instance, Fig. 2.10 is a RADARSAT image showing wave patterns in the Pacific Ocean around Point Reyes, California.

The European Space Agency (ESA) launched its first Earth-observing satellite, ERS-1, in 1991, followed by ERS-2 in 1995 and Envisat-1 in 2002 (the latter two are still operational.) Envisat-1 has nine on-board instruments, including the Medium Resolution Imaging Spectrometer (MERIS). As noted earlier, one of the main applications of the MERIS sensor has been for analyzing ocean color

Fig. 2.10 RADARSAT image recorded near Point Reyes, California. Image courtesy of NASA

Fig. 2.11 MERIS image, captured in August 2003, of the coastline of Bangladesh. Image courtesy of the European Space Agency

changes as an indicator of water quality (Cui et al. 2010). For example, Fig. 2.11 is a MERIS image of the coastline of Bangladesh, showing extensive sediments flowing into the Bay of Bengal.

Several nations outside North America and Europe have also established successful satellite programs. For example, the Indian Space Research Organization (ISRO) has constructed and launched 18 Earth-observing satellites, starting with Indian Resources Satellite (IRS) 1A in 1988. Its latest satellite, Resourcesat-2, carries three multispectral sensors with differing spatial resolutions: the 5.8-m, three-spectral-band Linear Imaging Self Scanner (LISS)-4; the 23.4-m, 4-band Linear Imaging Self Scanner (LISS)-3; and the 56-m, four-band Advanced Wide

Field Sensor (AWiFS). Together, these three sensors offer a high degree of analytical flexibility (Seshadri et al. 2005), making the satellite's data potentially suitable for a variety of tasks, as demonstrated by the use of Resourcesat imagery for studying coastal dynamics and water quality (Rajawat et al. 2007) and monitoring snow cover (Kulkarni et al. 2006).

The China-Brazil Earth Resources Satellite (CBERS) program was established by a cooperative agreement between the two countries in 1988. The CBERS-2B satellite, launched in 2007, carries three instruments, including a medium-resolution (20-m), multispectral charge coupled device (CCD) camera, which has been suggested as a low-cost supplement or alternative to other medium-resolution sensors such as Landsat ETM+ or Resourcesat-2's LISS-3 (Ponzoni and Albuquerque 2008). For example, Redo (2012) described a study of deforestation in Bolivia over a 33-year period (1975–2008), where data from multiple Landsat missions (i.e., MSS, TM, and ETM+ imagery) were combined with data from CBERS-2 and CBERS-2B to analyze a 63,000-km^2 area known as the Corredor Bioceánico.

The Japanese Aerospace Exploration Agency (JAXA) was formed in 2003 from a merger of three organizations: the National Space Development Agency of Japan (NASDA), the National Aerospace Laboratory (NAL), and the Institute of Space and Aeronautical Science (ISAS). One of JAXA's ongoing missions is the Greenhouse Gases Observing Satellite (GOSAT), or "Ibuki". Launched in 2009, GOSAT is the first satellite designed to remotely measure atmospheric concentrations of carbon dioxide (CO_2) and methane (CH_4) near Earth's surface (Morino et al. 2010; Kuze et al. 2009).

Commercial Satellites

Spot Image is a public company started by the French Space Agency (CNES) in 1982 (and now a subsidiary of EADS Astrium). Spot Image manages the SPOT Earth-observing satellites. The first satellite in the series, SPOT-1, was launched in 1986; SPOT-4 (launched in 1998) and SPOT-5 (launched in 2002) are currently in operation. Both SPOT-4 and SPOT-5 carry a "high-resolution" VNIR (HRVIR) sensor similar in capability to Landsat ETM+ (see Table 2.1), as well as a coarse-resolution VEGETATION sensor intended for regional mapping studies (Stibig et al. 2007). Unlike the Landsat-mounted sensors, the SPOT sensors are configured to permit off-nadir viewing (Jensen 2005), which can reduce revisit time from 26 days (i.e., the satellites' orbit cycle) to 2–3 days for the HRVIR sensor and one day for the VEGETATION sensor.

The SPOT-5 satellite also carries two High-Resolution Geometrical (HRG) instruments. Images from these 5-m panchromatic sensors have proven sufficient for fine-scale analyses such as the automatic detection of ships for monitoring of fisheries (Corbane et al. 2008). Furthermore, the two HRG sensors can be operated together in "super mode" to generate 2.5-m panchromatic imagery (Pasqualini et al. 2005).

The success of Spot Image laid the groundwork for the other commercially operated satellites that, starting with IKONOS in 1999, have provided panchromatic and multispectral imagery with very high spatial resolutions. (Indeed, in keeping with the trend, Spot Image's forthcoming Pléiades satellite will provide 0.5-m panchromatic and 2-m multispectral data.) Through a series of mergers and acquisitions, two U.S. companies have become the main contemporary providers of high-spatial-resolution imagery: GeoEye, which manages the IKONOS and GeoEye-1 satellites; and DigitalGlobe, which operates the Quickbird and WorldView-2 satellites (see Table 2.1 for sensor specifications). As noted earlier in this chapter, there are clearly many potential applications for these data. Nevertheless, it is important to acknowledge that such images are not well suited to standard classification techniques (e.g., maximum likelihood classification), primarily because objects and areas of interest are often represented by multiple pixels with fairly high variability in their spectral values (e.g., due to shadows) (Blaschke 2010; Yu et al. 2006). Instead, object-oriented classification techniques (see Chap. 3) are increasingly popular for application to high-spatial-resolution images. Another issue for commercial satellite imagery is the cost to the user, especially given the free availability of other satellite imagery (e.g., Landsat) that, while of coarser spatial resolution, may be sufficient for analysis. In any case, users of remotely sensed data should carefully consider the objectives of their particular projects when selecting the imagery most likely to meet those objectives.

References

A. Apan, A. Held, S. Phinn, J. Markley, Detecting sugarcane 'orange rust' disease using EO-1 Hyperion hyperspectral imagery. Int. J. Remote Sens. **25**, 489–498 (2004)

G.P. Asner, K.B. Heidebrecht, Imaging spectroscopy for desertification studies: comparing AVIRIS and EO-1 Hyperion in Argentina drylands. IEEE Trans. Geosci. Remote. Sens. **41**, 1283–1296 (2003)

T. Blaschke, Object based image analysis for remote sensing. J. Photogramm. Remote Sens. **65**, 2–16 (2010)

P.K.E. Campbell, B.N. Rock, M.E. Martin, C.D. Neefus, J.R. Irons, E.M. Middleton, J. Albrechtova, Detection of initial damage in Norway spruce canopies using hyperspectral airborne data. Int. J. Remote Sens. **25**, 5557–5583 (2004)

S.A. Carn, J.S. Pallister, L. Lara, J.W. Ewert, S. Watt, A.J. Prata, R.J. Thomas, G. Villarosa, The unexpected awakening of Chaitén volcano, Chile Eos **90**, 205–206 (2009)

J. Caylor, Aerial photography in the next decade. J. For. **98**(6), 17–19 (2000)

G. Chander, D.J. Meyer, D.L. Helder, Cross calibration of the Landsat-7 ETM+ and EO-1 ALI sensor. IEEE Trans. Geosci. Remote Sens. **42**, 2821–2831 (2004)

M.E. Charlton, A.R.G. Large, I.C. Fuller, Application of airborne LiDAR in river environments: the river Coquet, Northumberland, UK. Earth Surf. Proc. Land. **28**, 299–306 (2003)

J. Chen, G.F. Hepner, Investigation of imaging spectroscopy for discriminating urban land covers and surface materials, in *Proceedings of the 2001 AVIRIS Earth Science and Applications Workshop*, Palo Alto, CA. NASA JPL Publication 02–1. 2001. http://popo.jpl.nasa.gov/docs/work-shops/01_docs/2001Chen_web.pdf

Y. Chen, P. Shi, T. Fung, J. Wang, X. Li, Object-oriented classification for urban land cover mapping with ASTER imagery. Int. J. Remote Sens. **28**, 4645–4651 (2007)

C. Corbane, F. Marre, M. Petit, Using SPOT-5 HRG data in panchromatic mode for operational detection of small ships in tropical area. Sensors **8**, 2959–2973 (2008)

T. Cui, J. Zhang, S. Groom, L. Sun, T. Smyth, S. Sathyendranath, Validation of MERIS ocean-color products in the Bohai Sea; A case study for turbid coastal waters. Remote Sens. Environ. **114**, 2326–2336 (2010)

L.S. Galvão, A.R. Formaggio, E.G. Couto, D.A. Roberts, Relationships between the mineralogical and chemical composition of tropical soils and topography from hyperspectral remote sensing data. ISPRS J. Photogramm. Remote Sens. **63**, 259–271 (2008)

R.M. Goldstein, T.P. Barnett, H.A. Zebker, Remote sensing of ocean currents. Science **246**, 1282–1285 (1989)

J.C. Harsanyi, C.-I. Chang, Hyperspectral image classification and dimensionality reduction: an orthogonal subspace projection approach. IEEE Trans. Geosci. Remote Sens. **32**, 779–785 (1994)

D.B. Hester, H.I. Cakir, S.A.C. Nelson, S. Khorram, Per-pixel classification of high spatial resolution satellite imagery for urban land-cover mapping. Photogramm. Eng. Remote Sens. **74**, 463–471 (2008)

D.B. Hester, S.A.C. Nelson, H.I. Cakir, S. Khorram, H. Cheshire, High-resolution land cover change detection based on fuzzy uncertainty analysis and change reasoning. Int. J. Remote Sens. **31**, 455–475 (2010)

J.R. Jensen, *Introductory Digital Image Processing: A Remote Sensing Perspective.*, 3rd edn. (Prentice Hall, Upper Saddle River, 2005), p. 526

M.N. Jha, J. Levy, Y. Gao, Advances in remote sensing for oil spill disaster management: state-of-the-art sensors technology for oil spill surveillance. Sensors **8**, 236–255 (2008)

J.A. Johannessen, B. Chapron, F. Collard, V. Kudryavtsev, A. Mouche, D. Akimov, K.-F. Dagestad, Direct ocean surface velocity measurements from space: Improved quantitative interpretation of Envisat ASAR observations. Geophys. Res. Lett. **35**, L22608 (2008)

V. Klemas, Tracking oil slicks and predicting their trajectories using remote sensors and models: case studies of the Sea Princess and Deepwater Horizon oil spills. J. Coastal Res. **26**, 789–797 (2010)

F.A. Kruse, J.W. Boardman, J.F. Huntington, Comparison of airborne hyperspectral data and EO-1 Hyperion for mineral mapping. IEEE Trans. Geosci. Remote Sen. **41**, 1388–1400 (2003)

A.V. Kulkarni, S.K. Singh, P. Mathur, V.D. Mishra, Algorithm to monitor snow cover using AWiFS data of Resourcesat-1 for the Himalayan region. Int. J. Remote Sens. **27**, 2449–2457 (2006)

A. Kuze, H. Suto, M. Nakajima, T. Hamazaki, Thermal and near infrared sensor for carbon observation Fourier-transform spectrometer on the Greenhouse Gases Observing Satellite for greenhouse gases monitoring. Appl. Opt. **48**, 6716–6733 (2009)

T. Lillesand, R. Kiefer, J. Chipman, *Remote Sensing and Image Interpretation*, 6th edn. (Wiley, New York, 2008), p. 763

K. Lim, P. Treitz, M. Wulder, B. St-Onge, M. Flood, LiDAR remote sensing of forest structure. Prog. Phys. Geogr. **27**, 88–106 (2003)

Z. Liu, A. Omar, M. Vaughan, J. Hair, C. Kittaka, Y. Hu, K. Powell, C. Trepte, D. Winker, C. Hostetler, R. Ferrare, R. Pierce, CALIPSO lidar observations of the optical properties of Saharan Dust: a case study of long-range transport. J. Geophys. Res. **113**, D07207 (2008)

T.R. Loveland, B.C. Reed, J.F. Brown, D.O. Ohlen, Z. Zhu, L. Yang, J.W. Merchant, Development of a global land cover characteristics database and IGBP DISCover from 1 km AVHRR data. Int. J. Remote Sens. **21**, 1303–1330 (2000)

D. Massonnet, K.L. Feigl, Radar interferometry and its application to changes in Earth's surface. Rev. Geophys. **36**, 441–500 (1998)

J.L. Morgan, S.E. Gergel, N.C. Coops, Aerial photography: a rapidly evolving tool for ecological management. Bioscience **60**, 47–59 (2010)

I. Morino, O. Uchino, M. Inoue, Y. Yoshida, T. Yokota, P.O. Wennberg, G.C. Toon, D. Wunch, C.M. Roehl, J. Notholt, T. Warneke, J. Messerschmidt, D.W.T. Griffith, N.M. Deutscher, V. Sherlock, B. Connor, J. Robinson, R. Sussman, M. Rettinger, Preliminary validation of

column-averaged volume mixing ratios of carbon dioxide and methane retrieved from GOSAT short-wavelength infrared spectra. Atmospheric. Meas. Tech. Discuss. **3**, 5613–5643 (2010)
S. Moulin, L. Kergoat, N. Viovy, G. Dedieu, Global-scale assessment of vegetation phenology using NOAA/AVHRR satellite measurements. J. Clim. **10**, 1154–1170 (1997)
National Oceanic and Atmospheric Administration (NOAA), GOES Spacecraft Status Main Page [web page]. NOAA National Environmental Satellite, Data, and Information Service (NESDIS), Office of Satellite Operations (2011), http://www.oso.noaa.gov/goesstatus/
V. Pasqualini, C. Pergent-Martini, G. Pergent, M. Agreil, G. Skoufas, L. Sourbes, A. Tsirika, Use of SPOT 5 for mapping seagrasses: An application to *Posidonia oceanica*. Remote Sens. Environ. **94**, 39–45 (2005)
F.J. Ponzoni, B.F.C. Albuquerque, Pre-launch absolute calibration of CCD/CBERS-2B sensor. Sensors **8**, 6557–6565 (2008)
A.S. Rajawat, M. Gupta, B.C. Acharya, S. Nayak, Impact of new mouth opening on morphology and water quality of the Chilika Lagoon—a study based on Resourcesat-1 LISS-III and AWiFS and IRS-1D LISS-III data. Int. J. Remote Sens. **28**, 905–923 (2007)
D. Redo, Mapping land-use and land-cover change along Bolivia's Corredor Bioceánico with CBERS and the Landsat series: 1975–2008. Int. J. Remote Sens. 33, 1881–1904 (2012)
S.E. Reutebuch, H.-E. Andersen, R.J. McGaughey, Light detection and ranging (LIDAR): an emerging tool for multiple resource inventory. J. For. **103**, 286–292 (2005)
J. Rogan, D.M. Chen, Remote sensing technology for mapping and monitoring land-cover and land-use change. Prog. Plan. **61**, 301–325 (2004)
T. Schmugge, A. French, J.C. Ritchie, A. Rango, H. Pelgrum, Temperature and emissivity separation from multispectral thermal infrared observations. Remote Sens. Environ. **79**, 189–198 (2002)
K.S.V. Seshadri, M. Rao, V. Jayaraman, K. Thyagarajan, K.R. Sridhara Murthi, Acta Astronautica **57**, 534–539 (2005)
N.M. Short, The remote sensing tutorial [web site]. National Aeronautics and Space Administration (NASA), Goddard Space Flight Center (2010), http://rst.gsfc.nasa.gov/
H.-J. Stibig, A.S. Belward, P.S. Roy, U. Rosalina-Wasrin, S. Agrawal, P.K. Joshi, Hildanus, R. Beuchle, S. Fritz, S. Mubareka, C. Giri, A land-cover map for South and Southeast Asia derived from SPOT-VEGETATION data. J. Biogeogr 34: 625–637 (2007)
R. Stöckli, P.L. Vidale, European plant phenology and climate as seen in a 20-year AVHRR land-surface parameter dataset. Int. J. Remote Sens. **25**, 3303–3330 (2004)
USDA Farm Service Agency (FSA), Imagery programs—NAIP imagery [web site]. U.S. Department of Agriculture, Farm Service Agency, Aerial Photography Field Office (2010), http://www.fsa.usda.gov/FSA/apfoapp?area=home&subject=prog&topic=nai
B. Weber, C. Olehowski, T. Knerr, J. Hill, K. Deutschewitz, D.C.J. Wessels, B. Eitel, B. Büdel, A new approach for mapping of Biological Soil Crusts in semidesert areas with hyperspectral imagery. Remote Sens. Environ. **112**, 2187–2201 (2008)
D.L. Williams, S. Goward, T. Arvidson, Landsat: yesterday, today, and tomorrow. Photogramm. Eng. Remote Sens. **72**, 1171–1178 (2006)
Q. Yu, P. Gong, N. Clinton, G. Biging, M. Kelly, D. Schirokauer, Object-based detailed vegetation classification with airborne high spatial resolution remote sensing imagery. Photogramm. Eng. Remote Sens. **72**, 799–811 (2006)

Relevant websites

NASA's Visible Earth, highlighting numerous application examples of satellite-based sensors: http://visibleearth.nasa.gov
Landsat image archive: http://landsat.usgs.gov/
Canadian Space Agency (CSA): http://www.asc-csa.gc.ca

European Space Agency (ESA): http://www.esa.int
Indian Space Research Organization (ISRO): http://www.isro.org
China-Brazil Earth Resources Satellite (CBERS) Program: http://www.cbers.inpe.br/en/index_en.htm
Japan Aerospace Exploration Agency (JAXA): http://www.jaxa.jp/index_e.html
EADS Astrium (Spot Image): http://www.astrium-geo.com
SPOT VEGETATION Free Distribution Site: http://free.vgt.vito.be/
DigitalGlobe: http://www.digitalglobe.com
GeoEye: http://www.geoeye.com

http://www.springer.com/978-1-4614-3102-2

Remote Sensing

Khorram, S.; Koch, F.H.; van der Wiele, C.F.; Nelson, S.A.C.

2012, VII, 134 p. 76 illus., 31 illus. in color., Softcover
ISBN: 978-1-4614-3102-2